Fractal Neural Network: A new ensemble of fractal geometry and convolutional neural networks for the classification of histology images

Fractal Neural Network: a new ensemble of fractal geometry and convolutional neural networks for the classification of histology images

Guilherme Freire Roberto[a,*], Alessandra Lumini[b], Leandro Alves Neves[c], Marcelo Zanchetta do Nascimento[a]

[a] *Faculty of Computation (FACOM) - Federal University of Uberlândia (UFU), Av. João Naves de Ávila 2121, BLB, 38400-902, Uberlândia, MG, Brazil*
[b] *Department of Computer Science and Engineering (DISI) - University of Bologna, Via dell'Università 50, 47521, Cesena, FC, Italy*
[c] *Department of Computer Science and Statistics (DCCE), São Paulo State University (UNESP), R. Cristóvão Colombo, 2265, 15054-000, São José do Rio Preto, SP, Brazil*

Abstract

Classification of histology images is a task that has been widely explored on recent computer vision researches. The most studied approach for this task has been the application of deep learning through CNN models. However, the use of CNN in the context of histological images classification has yet some limitations such as the need of large datasets, the slow training time and the difficult to implement a generalized model able to classify different types of histology tissue. In this paper, we propose an ensemble model based on handcrafted fractal features and deep learning that consists on fusing the classification of two CNN by applying the sum rule. We apply feature extraction to obtain 300 fractal features from different histological datasets. These features are reshaped into a $10 \times 10 \times 3$ matrix in order to compose an artificial image that is given as input to the first CNN. The second CNN receives as input the correspondent original image. After combining the results of both

*Faculty of Computation (FACOM) - Federal University of Uberlândia (UFU), Av. João Naves de Ávila 2121, BLB, 38400-902, Uberlândia, MG, Brazil. Tel.: +55 34 32394470

Email addresses: guilhermefroberto@gmail.com (Guilherme Freire Roberto), alessandra.lumini@unibo.it (Alessandra Lumini), leandro@ibilce.unesp.br (Leandro Alves Neves), marcelo.zanchetta@gmail.com (Marcelo Zanchetta do Nascimento)

CNN, we were able to obtain accuracies that range from 89.66% up to 99.62% on five different datasets. Moreover, our model was able to classify images from datasets with imbalanced classes, without the need of images having the same resolution, and in a relative fast training time. We also verified that the obtained results are compatible with the most recent and relevant studies recently published in the context of histology image classification.

Keywords: deep learning, fractal features, classification ensemble, histology images

1. Introduction

Histopathology consists on the analysis of histological tissue and the study of how diseases affect the cells. Usually, a pathologist performs this analysis by observing histology slides through a digital microscope [7]. However, this task is prone to errors as evaluation is often subjective and dependent on the pathologist's experience, which may lead to misdiagnosis [38].

In order to provide support to pathologists, several computer vision techniques have been applied on images obtained from histology slides. These techniques consist on performing a series of evaluations on the input images and then provide a classification based on pre-defined classes, such as benign or malignant. This is a complex procedure, often refferred as computer aided-diagnosis (CAD), which can be split into several stages, from image acquisition, going through pre-processing, segmentation, feature extraction, feature selection and classification [27]. Therefore, a CAD system is an important tool that provides a second view to the pathologist, increasing the diagnosis accuracy and reducing the amount of time and physicians required to label large amounts of medical exams [18]. In this paper, we focus on the feature extraction and classification stages of a CAD system for histological image analysis.

Different techniques can be applied to extract handcrafted features from these images. Among the most recently researched techniques, we can cite local binary pattern (LBP), gray level co-occurrence matrix (GLCM), speeded up robust features (SURF) or fractal geometry, which were applied for kidney tissue analysis [53], breast cancer classification [64], colon cell nuclei detection [2] and lymphoma classification [47], respectively. However, the main research focus for this area in recent years has been the application of

deep learning approaches, more specifically, the use of convolutional neural networks (CNN).

CNN have shown to be efficient for the classification of objects, mainly in multiclass problems [28, 24]. However, these relevant results are not as often in the context of histological images [10, 59, 4]. One of the reasons is that CNN require large sets for training, given that a major part of the public histological datasets available contain a limited number of samples [63]. To handle this situation, more data is generated for training by applying rotation, mirroring or region cutting on the images. Nonetheless, this data augmentation raises even more the high computational cost of CNN [32].

One of the possible solutions to reduce processing time consists in simplifying the network architecture by reducing the amount of layers. However, the removal of deeper layers may hinder the image analysis from a global perspective [4], which may compromise the network performance. Some alternative approaches, like hybrid networks, have been explored. These approaches associate non-deep learning techniques such as Gabor filters or LBP operators with the convolution operations of CNN, which allows to replace some of the network's layers [28, 24]. Other approaches aim to achieve a lower processing time by reducing the images' dimensionality. In [29], the authors applied Haar-wavelet decomposition on breast histology images and used the decomposed images as input to a CNN.

Recent researches have shown that a fusion of handcrafted features with deep learning models can enhance common approaches [40]. The application of fractal features, which have provided relevant results in the context of histological images classification [46, 48], could also be associated to hybrid CNN. In [62], CNN were applied to extract values from an invariant fractal dimension filter for detecting object curves in grayscale images. The authors in [37] applied multifractal analysis to quantify and detect breast cancer, classifying the generated feature vectors using deep learning. However, an approach similar to the proposed by [29], wherein the CNN receives as input secondary images generated by a specific technique has not yet been experimented in the fractal geometry context. Moreover, methods that directly associate fractal geometry with CNN through an ensemble for the classification of histological images were not found in the literature.

In this paper, we propose a novel approach, which we name as Fractal Neural Network (FNN), to classify histological images through the association of fractal geometry and CNN. In our proposal, fractal features are extracted from the histology images and then rearranged in order to gen-

erate an artificial RGB feature image. Both this artificial image and the correspondent original image are given as input to a CNN ensemble, wherein a classification based on the sum rule outputs the class prediction. This new method provides the following contributions to the literature:

1. double-CNN classification ensemble wherein an image generated from handcrafted fractal features and the respective regular image are given as input to a CNN;
2. An adaptive method that is able to classify different sets of histological images, including datasets with imbalanced classes, few samples and varying image dimensions;
3. The combination of different fractal measures to provide a set of features capable of describing the image's properties;
4. A deep learning model that requires a small number of training epochs, even when classifying new types of histology images.

In the second section of this paper, recent researches regarding the classification of histological images are discussed. In Section 3, we provide a technical background on the use of fractal geometry for feature extraction of color images. The proposed methodology is presented on Section 4, and in Section 5, the results obtained by applying the method on the tested datasets are presented and discussed. Finally, we conclude the paper at Section 6, with an overview of the obtained results and suggestions for future researches.

2. Related Work

Plenty of advances have been achieved by researchers on the field of medical image classification recently, wherein deep learning approaches have been playing a major role on such improvements mainly on the feature extraction and classification stages of a CAD system.

2.1. Breast Tumors Classification

Breast cancer is a disease that initially starts with a tumor in the breast area but can later grow to surrounding tissues. This is the most common cancer type among women, although it also affects men. According to the Nacional Cancer Institute, 276,480 new cases and 42,170 deaths are expected in the United States for 2020 [17]. Due to high incidence, breast cancer detection became an important focus on computer vision research.

In [13], an artificial neural network composed by two modules was built to classify 58,000 patches with dimensions 15×15 of benign and malignant breast tumors. The first module performs an unsupervised feature extraction based on stacked denoising auto encoder. The second part, consists of a softmax classifier. This approach was able to provide accuracies of 98.27% and 90.54% for the detection of benign and malignant tumors, respectively. Multiple instance classification have also recently provided relevant results for the classification of breast tumors. Using a spatial decomposition technique that produces spatial and color components corresponding to 2nd and 3rd dimension of data tensors related to the input images, the authors in [44] were able to achieve an accuracy of 84.67% using a multiple instance classifier. Their method performed faster than other common approaches and could also obtain an accuracy of 79.33% even with 90% of missing data. Handcrafted image features have also been used as complementary to deep learning approaches. In [64], nuclei segmentation of breast tumors is performed through the application of a CNN. Then, texture features obtained from different handcrafted approaches are extracted from the segmented images and given as input to an SVM classifier. After applying the Relief feature selection method, the method was able to obtain an accuracy of 96.7%. In [31], the authors used data-augmentation to significantly increase the number of samples of the breast cancer dataset by generating 112×112 sized patches. To improve classification, the authors applied a simple six-layer CNN to remove mislabeled patches. After associating multiscale feature extraction with a CNN classifier, an accuracy of 100% was obtained.

2.2. Colorectal Tumors Classification

Colorectal cancer consists on the growth of malignant polyps in the colon or rectum area. This is the fourth most common type of cancer, with 147,950 new cases and 53,200 deaths expected for 2020 in the United States [17]. Several researches have been published in recent years aiming to improve the automated diagnosis of this type of cancer.

In [11], the authors used a 31-layers CNN to perform the classification of colorectal histological images, achieving accuracies of 93.24% and 96.97% for 5-class and 2-class classification respectively. Similar results were obtained in [51] when classifying 4 categories of colorectal tumors with a smaller network (12 layers), wherein an accuracy of 93.28% was obtained after 400 epochs of training. Furthermore, some researchers have been recently exploring approaches that consist of ensembles of different CNN models. The authors of

[5], for instance, first applied color normalization on the images of the colorectal dataset. Then, the normalized images were given as input to an U-Net CNN in order to perform segmentation, aiming to remove non-glandular areas. A different CNN model (GoogLeNet) was used to classify the segmented images. This approach provided an accuracy of 85%. An ensemble of different CNN was also published by [57] for the detection of colorectal tumors. The authors developed an approach based on generative adversarial networks (GAN) wherein the generator was implemented as an U-Net and the discriminator is a standard CNN. With 3,000 patches of colorectal tumor images available, the method provided an F-score of 0.940. According to the authors, this approach deals well with class imbalance, due to its capacity to retrain the network when new classes are added using the CNN Inception v3.

2.3. Non-Hodgkin Lymphomas Classification

Lymphomas are a type of cancer that affects cells of the immunological system, wherein the most common occurrence is the non-Hodgkin lymphoma (NHL). According to statistics, 77,240 new cases and 19,940 deaths caused by NHL are expected for 2020 in the United States [17]. Although it accounts for only 3.3% of all cancer-related deaths, NHL are divided into categories, each one requiring specific treatments. Therefore, computer methods that are able to identify the NHL type are an important tool to provide support to pathologists [43].

In [22], NHL images were split into several 36×36 patches which were later cropped to 32×32 sub-patches using the Caffe framework, generating 825,000 training patches. These patches were given as input to a standard AlexNet architecture and an accuracy of 96.58% was achieved with the use of a voting scheme for classification. However, the use of deep learning techniques is not mandatory to obtain relevant results for such task, as shown by [25]. On this approach, the images were firstly converted into grayscale and then, 130 non-overlapped patches with size 100×100 were extracted from each image, resulting in a total of 48,620 patches. An unsupervised feature extraction method was applied along with ordinary texture approaches to extract 680 handcrafted features. These features were classified using a hierarchical 2-stages machine learning method, which resulted in an accuracy of 97.96%. In [6], the authors proposed a method that applies both deep learning and handcrafted features for NHL classification. On this approach, color, statistical and texture features were extracted from patches cropped

out of the original images and given as input at a random forest classifier. These patches were also used to feed a GoogLeNet CNN. Both the random forest and the CNN provided patch predictions which were processed using weighted sum to generate a final classification prediction. The obtained accuracy was of 99.10%. Fractal features have also provided relevant results on NHL classification recently. In [36], fractal geometry was used to extract multiscale and multidimensional features from RGB and LAB colored NHL images. The features extracted from the original images, without data-augmentation, are given as input to a polynomial classifier. For binary class classification, an accuracy of up to 97% was obtained.

2.4. Gender and Age Classification

Besides providing support to the diagnosis of diseases and differentiation of tumors, computer vision techniques applied on histological images can also serve as an indicator of age and gender. A set of images obtained from mice liver tissue has been explored recently for this task. In [3], the authors presented a novel deep learning approach named Texture-CNN. After applying this approach along with a voting classification scheme, accuracies of 99.1% and 98.2% were obtained for the classification of 2 gender and 4 aging classes respectively. However, handcrafted features have also provided excellent results in this dataset. [12] applied 3 statistical approaches for grey texture analysis, testing on different color spaces. After using a SVM to classify the generated features, an accuracy of 100% was obtained for both gender and aging classes. More recently, the authors in [39] proposed an ensemble of handcrafted features and deep learning approaches. Moreover, new data augmentation techniques based on principal component analysis and discrete cosine transform were also presented. Using an ensemble of 6 CNN models trained with different data augmentation approaches and a set of handcrafted features, the method was also able to obtain an accuracy of 100% for classifying gender and age from liver histological images.

Despite providing relevant results, most of these methods were implemented for specific classification tasks. There are few computer vision approaches that were able to perform well on different histological image categories [48, 39, 19, 52]. Moreover, both handcrafted fractal features [46, 48, 49] and CNN models [31, 6, 3] were able to provide high accuracy rates in several CAD systems for histopathology tasks. Therefore, an ensemble method that addresses both fractal geometry and deep learning, which is the core of our

proposal, could be able to improve these results when applied to different histology datasets.

3. Technical Background

3.1. Fractal Features

Fractal geometry is a concept designed for the study of shapes that could not be defined by euclidian geometry [35]. Shapes present in nature such as a coastline, clouds, trees or lightnings are examples of structures that don't have well-defined patterns. With fractal-based approaches, these structures can be represented by observations through different scales. In computer vision, such techniques are known as multiscale. Among the most common ones, we can highlight the box-counting [41] and the gliding-box [21] algorithms. The application of these algorithms consists in splitting the images onto different scales and then extracting features from each sub-image. For the representation of numerical features using fractal approaches, we have fractal dimension (FD), lacunarity (LAC) and percolation (PERC) as three of the most relevant. A multiscale and a multidimensional analysis of the image are performed in order to obtain these features.

One of the approaches available in the literature for multiscale analysis consists on the application of the gliding-box algorithm [21]. One of the main advantages of this approach is that it can be applied on datasets containing images with different resolutions, due to the fact that the output features are given in relation to the scale instead of being absolute values. This algorithm consists in placing a box β_i sized $L \times L$ on the left superior corner of the image, wherein L is given in pixels. This box glides through the image, one column and then one row at a time. After reaching the end of the image, the box is repositioned at the starting point and the value of L is increased by 2. On an image sized $H \times W$, the total number T of boxes β_i for a scale L is given by Equation 1:

$$T(L) = (H - L + 1) \times (W - L + 1) \quad | \quad L \leq min(H, W). \tag{1}$$

For each time the box β_i is moved, a multidimensional analysis of color similarity is performed for every pixel inside it. This is done by assigning the center pixel to a vector $f_c = r_c, g_c, b_c$, where r_c, g_c and b_c correspond to the color intensities of each of the RGB color channels of given pixel. The other pixels in the box are assigned to a vector $f_i = r_i, g_i, b_i$ and compared to the

center pixel by calculating a color distance Δ. On the proposed approach, the Chessboard (Δ_h), Euclidian (Δ_e) and Manhattan (Δ_m) distances are calculated according to Equations 2-4.

$$\Delta_h = max(|f_i(k_i) - f_c(k_c)|), k \in r, g, b. \tag{2}$$

$$\Delta_e = \sqrt{\sum_k \left(f_i(k_i) - f_c(k_c)\right)^2}, k \in r, g, b. \tag{3}$$

$$\Delta_m = \sum_k |f_i(k_i) - f_c(k_c)|, k \in r, g, b. \tag{4}$$

If the value of Δ corresponding to the distance between f_i and f_c is less than or equal to the scale L, then f_i is labeled as 1, otherwise f_i receives the label 0. An example of the pixels' labelling when a distance Δ is calculated for a box sized 3×3 is illustrated on Figure 1.

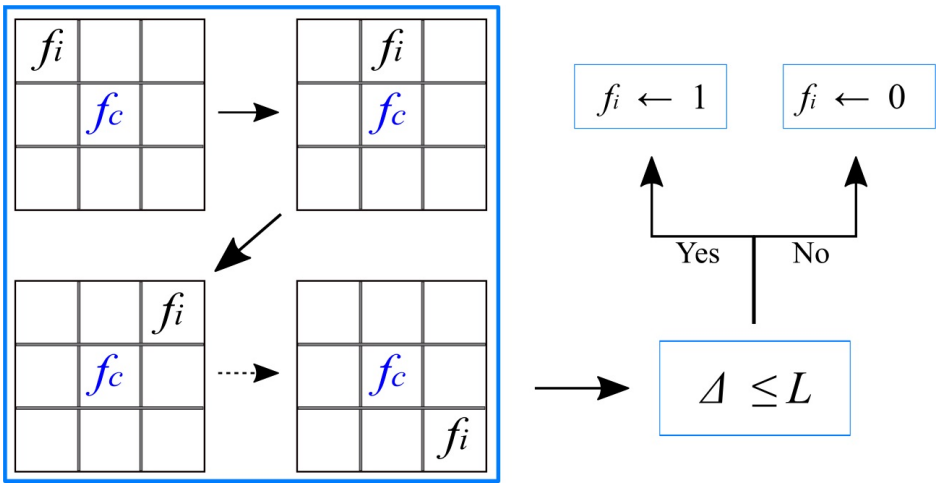

Figure 1: Labelling the pixels on a 3×3 by calculating a distance Δ.

This procedure converts a box that contains RGB values to one containing binary values. After performing this conversion for every box of every given L scale, a structure known as probability matrix is generated. Each element of the matrix corresponds to the probability P that m pixels on a scale L are labeled as 1 on each box. On Table 1, the visual representation of such matrix is presented. The matrix is normalized in a way that the sum of the elements in a column is equal to 1, as showed on Equation 5.

Table 1: Structure of the probability matrix.

	3	5	$\cdots$	L_{max}
1	$P(1,3)$	$P(1,5)$	$\cdots$	$P(1,L_{max})$
2	$P(2,3)$	$P(2,5)$	$\cdots$	$P(2,L_{max})$
$\vdots$	$\vdots$	$\vdots$	$\ddots$	$\vdots$
L^2	$P(L^2,3)$	$P(L^2,5)$	$\cdots$	$P(L^2,L_{max})$

$$\sum_{m=1}^{L^2} P(m,L) = 1, \forall L. \tag{5}$$

Noteworthy here that the probability matrix does not have the shape of an ordinary rectangular matrix, as the number of rows grows exponentially for each value of L. After the matrix is complete, the FD and LAC local values can be obtained.

3.1.1. Fractal Dimension

FD is the most common technique to evaluate the fractal properties of an image. This is a measure for evaluating the irregularity and the complexity of a fractal.

To obtain local FD features from the probability matrix, for each value of L, the FD denominated $D(L)$ is calculated according to the Equation 6:

$$D(L) = \sum_{m=1}^{L^2} \frac{P(m,L)}{m}. \tag{6}$$

3.1.2. Lacunarity

LAC is a measure complementary to FD and allows to evaluate how the space of a fractal is filled [20]. From the probability matrix, first and second order moments are calculated with the Equations 7 and 8.

$$\mu(L) = \sum_{m=1}^{L^2} mP(m,L). \tag{7}$$

$$\mu^2(L) = \sum_{m=1}^{L^2} m^2P(m,L). \tag{8}$$

The value of LAC for a scale L is given by $\Lambda(L)$, which is obtained according to the Equation 9:

$$\Lambda(L) = \frac{\mu^2(L) - (\mu(L))^2}{(\mu(L))^2}. \tag{9}$$

3.1.3. Percolation

PERC is a physical phenomenon that consists on the study of fluid properties on a porous media [15]. Such media is said to be percolating if a fluid can flow through the whole system, from the top to the bottom. In computer vision, this concept can be applied to verify the image porosity, or some cluster properties regarding pixel neighborhoods [49]. The first steps to obtain percolation features from a colored image follow the same procedures described for obtaining FD and LAC features. After calculating Δ, the generated binary matrices are given as input to a cluster labelling algorithm. Groups of nearby pixels that satisfied the criterion of the Δ distance are labelled in order to count the number of clusters on the image, as illustrated in Figure 2. The symbol * indicates pixels labelled as 1.

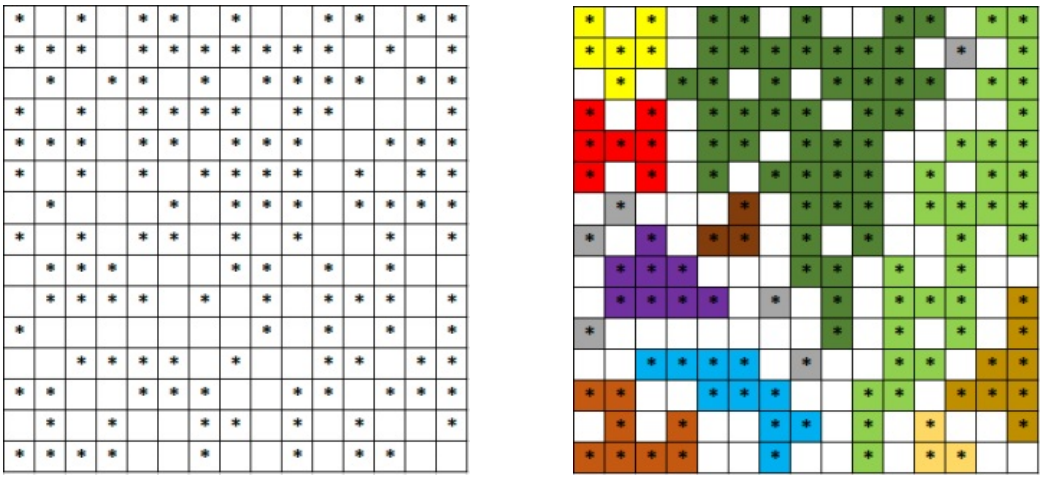

(a) (b)

Figure 2: Matrix before (a) and after (b) the application of a cluster labelling algorithm.

Let c_i be the number of clusters on a box β_i, the feature $C(L)$ that represents the average number of clusters per box on a scale L is given by Equation 10

$$C(L) = \frac{\sum_{i=1}^{T(L)} c_i}{T(L)}. \tag{10}$$

Another feature that can be obtained consists on the average coverage area of the largest cluster in a box and is given by $M(L)$. Let m_i be the size in pixels of the largest cluster of the box β_i. The feature $M(L)$ is given according to Equation 11:

$$M(L) = \frac{\sum_{i=1}^{T(L)} \frac{m_i}{L^2}}{T(L)}. \tag{11}$$

We can also verify whether a box β_i is percolating. This can be achieved due to a property that states a percolation threshold for different types of structures. In squared matrices (digital images), this threshold has the value of $p = 0.59275$ [8], which means that if the ratio between pixels labeled as 1 and pixels labeled as 0 is greater or equal than p, the matrix is considered as percolating. Let Ω_i be the number of pixels labeled as 1 in a box β_i with size $L \times L$, we determine whether such box is percolating according to Equation 12:

$$q_i = \begin{cases} 1, & \frac{\Omega_i}{L^2} \geqslant 0.59275. \\ \\ 0, & \frac{\Omega_i}{L^2} < 0.59275. \end{cases} \tag{12}$$

This results in a binary value for q_i, wherein 1 indicates that the box is percolating. The feature $Q(L)$ regards the average occurrence of percolation on a scale L and can be obtained as shown in Equation 13:

$$Q(L) = \frac{\sum_{i=1}^{T(L)} q_i}{T(L)}. \tag{13}$$

The number of obtained local features depends on the total of observation scales L. Considering that L ranges from 3 to L_{max} with an increment of 2, the amount of local features corresponds to $5 \times (\frac{L_{max}-3}{2} + 1)$ for each Δ. A summary of these features is shown in Table 2.

3.2. Convolutional Neural Networks

CNN are a special type of deep learning model that learns features from low- and high-level patterns on grid-shaped data [63]. The core of CNN

Table 2: Summary of the obtained local features.

FD	**LAC**	**PERC**		
$D(3)$	$\Lambda(3)$	$C(3)$	$Q(3)$	$M(3)$
$D(5)$	$\Lambda(5)$	$C(5)$	$Q(5)$	$M(5)$
$\vdots$	$\vdots$	$\vdots$	$\vdots$	$\vdots$
$D(L_{max})$	$\Lambda(L_{max})$	$C(L_{max})$	$Q(L_{max})$	$M(L_{max})$

are usually built from three types of layers: convolution; pooling; and fully connected layers. While the first two perform feature extraction, the later classifies these features and usually outputs a label to be assigned to the input data.

The convolution layers are the base structures of the network, hence the name CNN. These layers usually consist on a series of two operations. The first is convolution, a simple linear procedure that performs element-wise product between the input data and small arrays of numbers called kernels, which are the only learnable parameters in this type of layers. The second operation consists on passing the convolution output through a non-linear activation function. Different functions have been applied, although the Rectified Linear Unit (ReLU), which is given by $f(x) = max(0, x)$, became the most popular as it tends to reduce training time [30].

Pooling layers provides a downsampling operation that reduces the data dimensionality. This is usually done by selecting the maximum or sometimes the average value of an element in a patch and feeding it to the following layer. These pooling operations are performed in order not only to decrease the number of features but also to introduce a small invariance to translation and distortion of structures in the input data.

The fully connected layers consist on a series of one or more layers wherein every output is connected to every input of the following layer by a learnable weight. Usually, the last fully connected layer has the same number of nodes as the number of classes of the training dataset. In classification problems, its output corresponds to class probabilities, which are obtained by applying an activation function, such as softmax. The network's prediction is given by the class that obtained the highest probability value.

4. Methodology

4.1. Image Databases

We evaluated five histological image datasets. The first is the breast cancer dataset provided by the Center of Bio-Image Informatics from the University of California, Santa Barbara (UCSB) [14]. This dataset consists of 58 breast tissue images split into two groups: benign (32) and malignant (26). One example of each group is shown in Figure 3.

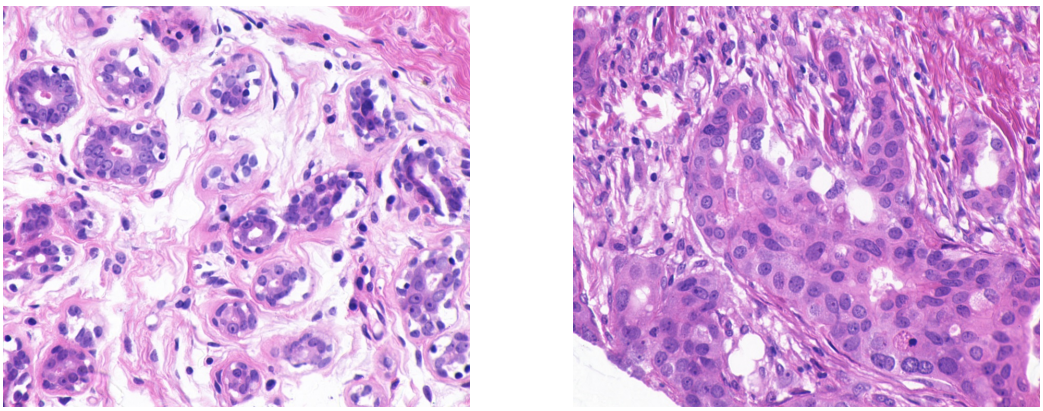

(a) (b)

Figure 3: Samples of a benign (a) and a malignant (b) case from the UCSB dataset.

The second dataset (CR) consists of 165 colorectal tissue images [54], also split into benign (74) and malignant (91) tumors. To acquire the images, histological sections were digitally photographed with a Zeiss MIRAX MIDI Slide Scanner with a scaled pixel resolution of $0.620\mu m$, which corresponds to a magnification of 20x. On Figure 4, examples from each class are illustrated.

The third dataset (NHL) is composed by 173 non-Hodgkin Lymphoma images divided into three classes: MCL - mantle cell lymphoma (99); FL - folicular lymphoma (62); and CLL - chronic lymphocyte leukemia (12). For the acquisition of the images, a light microscope Zeiss Axioscope with a 20x objective and a colored digital camera (AXio Cam MR5) were used. The obtained images were recorded without compression, with a resolution of 1388×1040 pixels, a 24 bit quantization ratio and the RGB color model. Regions of interest were later selected by a specialist [58]. This dataset was made publicly available by the National Cancer Institute and the National Institute on Aging [52].

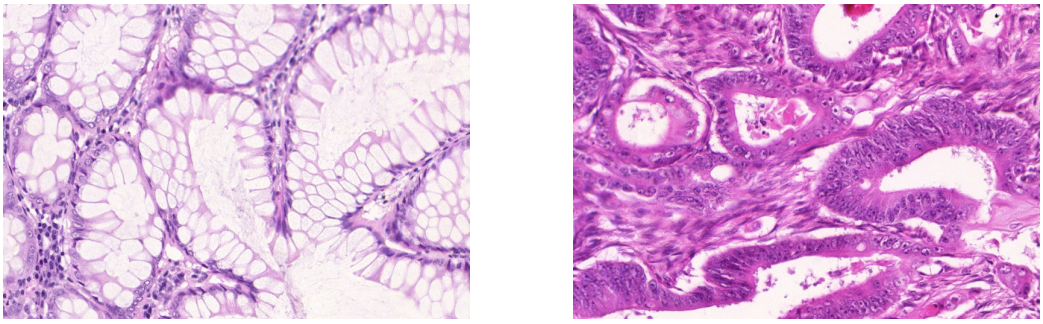

(a) (b)

Figure 4: Samples of a benign (a) and a malignant (b) case from the CR dataset.

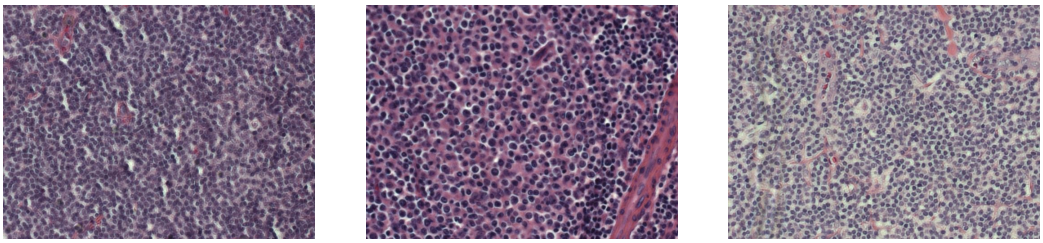

(a) (b) (c)

Figure 5: Samples of a CLL (a), a FL (b) and a MCL (c) case from the NHL dataset.

The two following datasets were both provided by the Atlas of Gene Expression in Mouse Aging Project (AGEMAP) and are composed by liver tissue obtained from mice [42]. The images were acquired by a Carl Zeiss Axiovert 200 microscope and 40x objective. All images have the same resolution of 417×312 pixels. The fourth dataset (LG) consists of 265 liver tissue images obtained from male (150) and female (115) mice on a caloric restriction diet. Examples of each class are illustrated on Figure 6. The fifth dataset (LA) consists of 529 images split in four classes, wherein each represents a different age group of female mice on ad-libitum diets: one (100), six (115), 16 (162) and 24 (152) months old. On Figure 7, one example of each age group is illustrated. An overview of all these datasets is presented on Table 3. In all five datasets, the tissue samples were stained with Hematoxylin and Eosin (H&E).

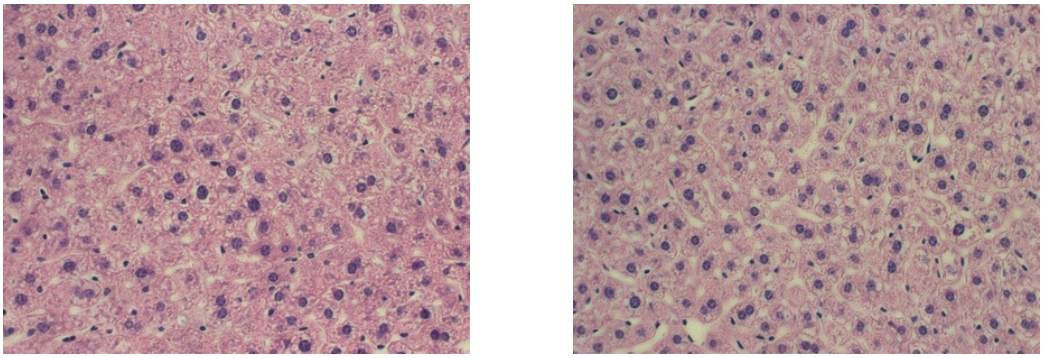

(a) (b)

Figure 6: Samples of liver tissue from male (a) and female (b) mice from the LG dataset.

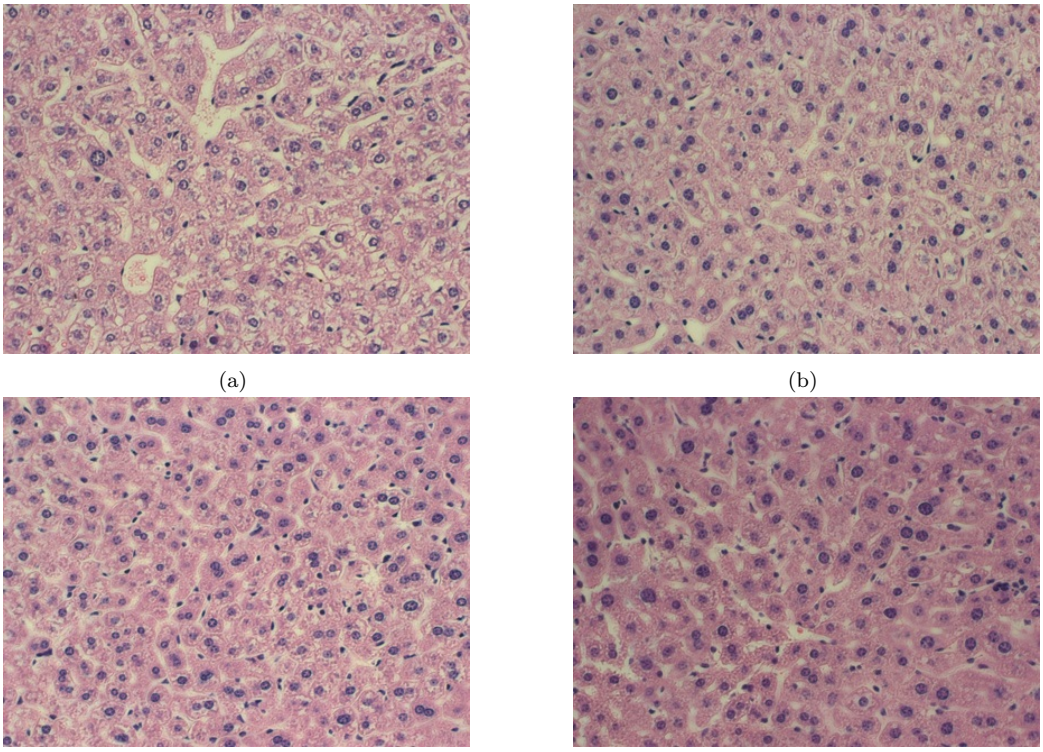

(a) (b)

(c) (d)

Figure 7: Samples of liver tissue from mice aged 1 month (a), 6 months (b), 16 months (c) and 24 months (d) from the LA dataset.

Table 3: Summary of the five tested datasets.

Dataset	Image	Classes	Samples	Resolution
UCSB [14]	Breast tumors	2	58	896×768
CR [54]	Colorectal tumors	2	165	from 567×430 to 775×522
NHL [52]	Non-Hodgkin Lymphoma	3	173	from 86×65 to 1388×1040
LG [42]	Liver tissue	2	265	417×312
LA [42]	Liver tissue	4	529	417×312

4.2. Method Overview

The proposed approach can be split into two modules. The first module performs the extraction of local features by applying the fractal techniques described in Section 3.1. The output of this module consist on a set of 300 features, which were obtained from calculating the FD, LAC and PERC local values from each of the three distances Δ evaluated. The second module is composed by 2 CNN whose goal is to perform classifications to obtain an array of probabilities.

The input of the first CNN, henceforth named F-CNN, consists on an artificial image generated from the features extracted on the first module. The set of local features is reshaped into a $10 \times 10 \times 3$ RGB image, which is a procedure based on [33]. The generated images are given as input to a CNN for classification. The second CNN, henceforth named O-CNN, receives as input the original image, wherein the class probabilities obtained from the classification of such image are summed to the respective class probabilities from the F-CNN. After this sum, the highest probability value indicates the class prediction. An overview of this approach is presented on Figure 8. Each step is described in details on the following sections.

4.3. Feature Extraction Module

The main stage of the proposed method consists in applying the techniques based on fractal geometry, described in Section 3.1, on the images under investigation. FD, LAC, and PERC local features are extracted using multiscale and multidimensional approaches.

After being given as input to the FNN, the image is divided into different scales, according to the gliding-box algorithm. Each perceptron of the first layer represents a different scale with value L. This layer's function consists simply in generating a set of matrices for every region of the image and every assigned value of L, which ranges from 3 to 41 with an increment of 2. We chose this value for L_{max} as it generates the exact number of features required

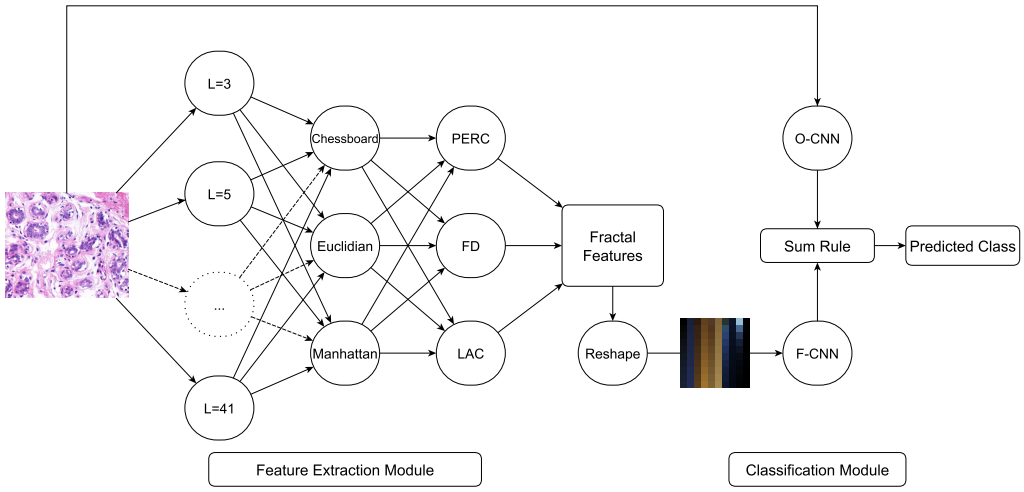

Figure 8: Overview of the proposed Fractal Neural Network model.

to provide a square image after applying the reshape procedure, which is ideal to avoid distortions when feeding the image to the F-CNN, and also due to the relevant classification results obtained with a similar value [46]. The generated matrices are given as input to the second layer, which is a representation of the multidimensional approach of the methods described on Section 3.1. In the proposed architecture, each perceptron performs the calculation of a different type of distance Δ between the pixels of the image.

The output of each perceptron in the second layer consists in a set of binary matrices, wherein the values labeled as 1 are pixels that matched the Δ criteria. These matrices are given as input to the perceptrons of the third layer, wherein the techniques described on Section 3.1 for obtaining local FD, LAC and PERC values are finally applied. The resulting output consists on a set of 300 local features, which serve as input to the next module of the network. Prior to being given as input to both CNN, the original and the fractal images are resized in order to match the required input dimensions.

4.4. Classification Module

On the proposed FNN, classification is performed by two CNN. Both CNN are fine-tuned on the deepest layer, as we applied transfer learning using models pre-trained on the ImageNet database [50] in order to increase the accuracy whilst reducing the training time.

4.4.1. Fractal Features CNN - F-CNN

In order to serve as input for the incoming CNN classification, the feature vectors generated on the previous layers of the network must be converted into feature matrices. In order to do so, the set of 300 features obtained from the calculation of each of the three distances Δ are arranged to compose a different dimension of the matrix, aiming to simulate RGB color channels. Therefore, we split the feature vector into three sub-vectors containing 100 features. These features are sequentially rearranged into a 10×10 matrix. The matrices generated by Δ_h, Δ_e and Δ_m correspond to the R, G and B color channels, respectively. In Figure 9, one example of each tested dataset is shown in order to illustrate the reshaping procedure.

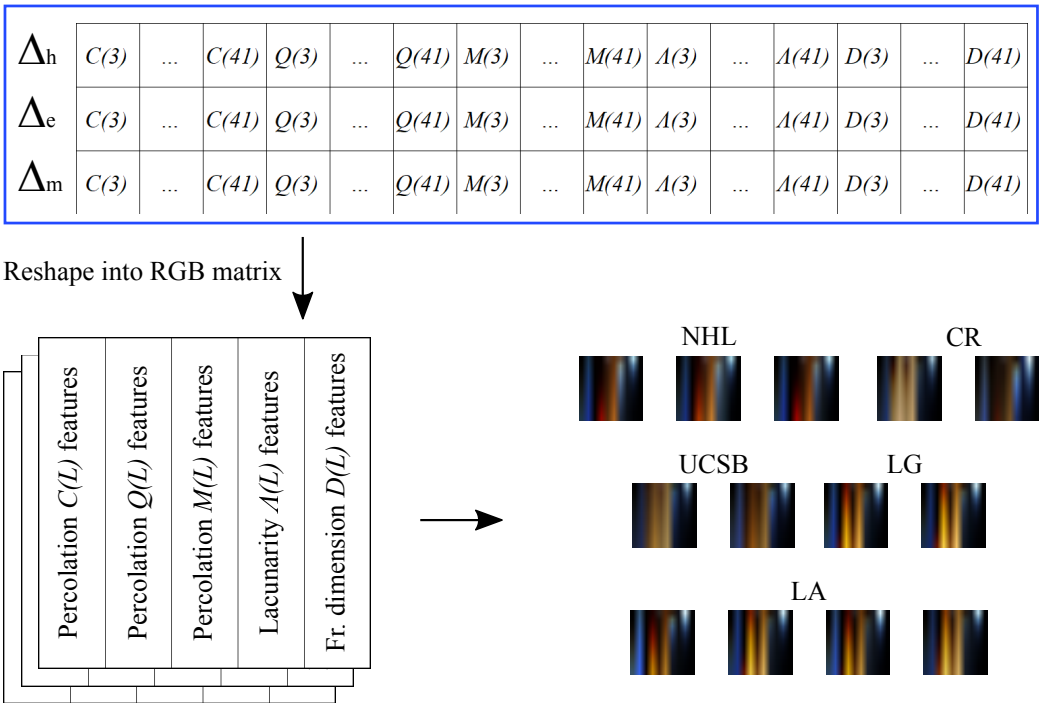

Figure 9: Illustration of the procedure to rearrange the local features in order to create a RGB image.

The generated images are given as input to the F-CNN, which outputs a score vector for each image indicating class probabilities.

4.4.2. Original Images CNN - O-CNN

In order to fully explore the classification power of a CNN, we chose to append a second CNN to the proposed architecture. The original images are given as input to this CNN and the class probabilities obtained from the output of the softmax layer are summed to the class probabilities obtained from the correspondent layer of the F-CNN where the images generated from fractal features were classified.

4.4.3. Transfer Learning

In order to reduce training time and achieve good results with few training epochs we chose to use transfer learning instead of training both CNN from scratch. Our proposed method applies network-based transfer learning [56], wherein the pre-trained network is partially reused and only the final layer is changed in order to match the number of classes. Therefore, we selected four CNN candidates that have provided relevant results in histology image classification recently [45, 34, 26] pre-trained on the ImageNet dataset. An overview of these four models is shown in Table 4.

Table 4: Selected pre-trained CNN models.

Model	Layers	Parameters	Input size
ResNet-50 [16]	50	2.6×10^7	$224 \times 224 \times 3$
ResNet-101 [16]	101	4.5×10^7	$224 \times 224 \times 3$
InceptionV3 [55]	48	2.4×10^7	$299 \times 299 \times 3$
Xception [9]	71	2.3×10^7	$299 \times 299 \times 3$

4.5. Performance Evaluation

In order to obtain the best possible results with the proposed method and properly evaluate these, we applied a testing approach divided in 4 stages.

Firstly, we evaluated which CNN model would be the most appropriate for the F-CNN and O-CNN slots in the proposed architecture. Then, we apply each of the CNN on the 5 datasets with the number of training epochs ranging from 1 to 10. This verification aims to determine the smaller number of epochs needed to obtain the highest accuracies. After these experiments, the proposed approach is applied on the datasets using the configuration results obtained from the previous tests. At last, we compare the proposed method with other common feature extraction techniques, analysing results

Table 5: Loss evaluation of different CNN models and time performance in seconds.

Dataset		ResNet-50	ResNet-101	InceptionV3	Xception
NHL	F-CNN	0.510	0.494	0.478	**0.385**
	O-CNN	0.767	0.585	0.497	**0.409**
	Time	**42.69**	85.79	87.58	77.01
CR	F-CNN	0.350	0.312	0.339	**0.269**
	O-CNN	**0.018**	0.022	0.045	0.043
	Time	**50.21**	91.26	93.82	83.37
UCSB	F-CNN	0.567	0.741	0.621	**0.556**
	O-CNN	0.318	**0.271**	0.305	0.606
	Time	**21.99**	39.65	39.01	29.76
LG	F-CNN	0.163	**0.118**	0.151	**0.118**
	O-CNN	**0.005**	0.017	**0.005**	0.041
	Time	**67.25**	133.84	139.99	128.66
LA	F-CNN	**0.175**	0.189	0.196	0.193
	O-CNN	0.048	0.128	**0.031**	0.051
	Time	**122.47**	247.67	259.65	247.22

obtained from using only the F-CNN as well as the ensemble with the O-CNN. To obtain these other features, we implemented the methods on Matlab R2019b, applied them on the same datasets and performed classification using the Rotation Forest classifier available at the software Weka 3.6.13. We chose this classifier due to its relevant results obtained from other researches on histology image classification [1, 48].

All tests were performed on a Intel Xeon Silver 4116 CPU at 2.10GHz with 128GB of RAM and a NVIDIA GeForce RTX 2080Ti embedded, using Matlab R2019b. Since some of the tested datasets have a small number of samples, we chose to apply 10-folds cross-validation in all testing stages in order to avoid problems such as overfitting.

5. Results and Discussion

Before testing the proposed model on its complete implementation, it was necessary to determine the CNN models to be assigned to the F-CNN and O-CNN slots. We tested the performance of four of the most popular CNN that have been applied on recent researches. On Table 5, the loss values for each dataset are presented as well as the average time in seconds required to train and classify the samples in 10 epochs.

We applied the Friedman non-parametrical test to verify whether the difference among the loss values were significant [23]. At $\alpha = 0.05$, we

Table 6: Accuracy values for the F-CNN with varying training epochs.

Epochs	NHL	CR	UCSB	LG	LA	Avg.
1	78.03%	77.58%	60.34%	68.68%	77.88%	72.50%
2	80.35%	78.79%	70.69%	81.13%	81.66%	78.52%
3	78.61%	83.03%	68.97%	91.32%	84.88%	81.36%
4	82.66%	83.64%	70.69%	88.68%	86.39%	82.41%
5	**84.97%**	**89.09%**	74.14%	93.21%	86.77%	85.63%
6	84.39%	86.67%	72.41%	89.81%	91.68%	84.99%
7	**84.97%**	88.48%	68.97%	90.94%	91.68%	85.01%
8	84.39%	88.48%	72.41%	91.70%	90.36%	85.47%
9	82.66%	86.06%	**79.31%**	95.09%	**93.57%**	**87.34%**
10	83.81%	86.06%	77.59%	**95.47%**	93.19%	87.23%

Table 7: Accuracy values for the O-CNN with varying training epochs.

Epochs	NHL	CR	UCSB	LG	LA	Avg.
1	83.82%	93.33%	56.90%	98.49%	92.82%	85.07%
2	87.28%	98.18%	58.62%	98.49%	95.27%	87.57%
3	89.02%	98.79%	68.97%	98.49%	96.03%	90.26%
4	90.75%	98.78%	72.41%	98.11%	96.68%	91.33%
5	90.75%	**100.00%**	75.86%	**99.62%**	98.11%	92.87%
6	88.44%	99.39%	79.31%	**99.62%**	97.16%	92.79%
7	90.17%	99.39%	74.14%	**99.62%**	98.49%	92.36%
8	**93.64%**	98.79%	81.03%	98.87%	98.68%	**94.20%**
9	89.60%	98.18%	**82.76%**	98.87%	99.05%	93.69%
10	88.44%	99.39%	75.86%	98.82%	**99.43%**	92.40%

obtained $P_k = 0.2073$ for the F-CNN and $P_k = 0.4144$ for the O-CNN, which indicates that there is not a significant difference when comparing the four tested CNN models. However, when comparing the time needed to perform training, the Friedman test indicated a significant difference ($P_k < 0.0001$) for all pairwise comparisons (Conover) involving the ResNet-50. Therefore, we chose the ResNet-50 to be assigned to both CNN slots of our proposed architecture not only due to its shorter training time, but also due to the relevant results recently obtained in the classification of histology images [45, 34, 60, 61].

Then, we tested the performance of each of the two CNN varying the number of training epochs. To prevent overfitting, and aiming to build a fast-training model, we chose to not go beyond 10 epochs for both CNN. The results are shown in Tables 6 and 7 for the F-CNN and the O-CNN respectively.

Table 8: Results obtained from the application of the proposed method.

	Accuracy	F-score
NHL	95.55%	0.864
CR	99.39%	0.994
UCSB	89.66%	0.895
LG	99.62%	0.996
LA	99.62%	0.996
Avg.	96.77%	0.949
SD.	4.334	0.058

From the results presented on Tables 6 and 7, it can be noted that the F-CNN is able to provide relevant results after 4 epochs. On the other hand, the O-CNN presented significant performance values with only 2 training epochs, providing accuracies above 85% for all datasets, with an exception for the breast tumor images, due to its small number of samples. Nevertheless, the best results were obtained with 9 and 8 training epochs for the F-CNN and O-CNN respectively. Therefore, these parameters were applied on the following tests.

We proceeded to apply the proposed FNN using the configuration parameters obtained on the previous tests in order to evaluate the performance when applied to the five histology images dataset. The detailed results are shown on Table 8.

These results show that the proposed method is able to perform well on the classification of histology images. With exception for the UCSB dataset, accuracies above 95% were obtained, which can be a indicator of the method's adaptability to different categories of histological tissue. Despite dealing with imbalanced classes on all datasets, the proposed method was also able to provide F-Measure values above 0.850 in all cases. It is also noteworthy the excellent results obtained for the CR, LG and LA, with performance values close to 1.0 for all evaluated metrics.

In order to verify how the proposed method fits among other computer vision approaches, we compare its performance with the results obtained by LBP, Haralick, PERC, LAC and FD features. It's important to highlight that the fractal features used for comparison in this test consist of common feature vectors that are given as input to machine learning algorithms, which differs from our approach of reshaping the fractal features into a RGB image and feeding it to a CNN. Firstly, we compared the individual performance of

Table 9: Accuracy values obtained by different computer vision methods.

	NHL	CR	UCSB	LG	LA
LBP	72.83%	67.27%	79.31%	80.75%	71.46%
Haralick	74.57%	73.94%	81.03%	89.43%	88.28%
PERC	**93.64%**	87.27%	**82.76%**	95.09%	93.57%
LAC	89.60%	66.67%	79.31%	86.04%	83.93%
FD	78.03%	59.39%	62.07%	58.49%	50.47%
F-CNN	82.66%	86.06%	79.31%	95.09%	93.57%
O-CNN	**93.64%**	**98.79%**	81.03%	**98.87%**	**98.68%**

Table 10: Accuracy values obtained by the application of a classification ensemble between the O-CNN and other techniques.

	NHL	CR	UCSB	LG	LA
LBP	83.24%	91.52%	82.76%	93.58%	89.41%
Haralick	87.28%	92.12%	82.76%	95.47%	92.25%
PERC	94.22%	97.58%	86.21%	**99.62%**	99.24%
LAC	94.22%	98.18%	86.21%	**99.62%**	98.87%
FD	91.91%	98.79%	82.76%	99.25%	99.05%
FNN	**95.55%**	**99.39%**	**89.66%**	**99.62%**	**99.62%**

these techniques without using any classification fusion or ensemble approach. Thus, we did not performed the ensemble scheme between the F-CNN and the O-CNN, as it is originally intended for our proposal. The results are shown in Table 9.

Without using any ensemble approach, the O-CNN, which consists simply on using a ResNet-50 for classifying the original images, provided the best results. An exception is made for the UCSB dataset, wherein the best results were provided by the PERC features. Moreover, apart from the FD, the fractal features performed better than the LBP and Haralick descriptors in most cases. It can also be noted that the proposed F-CNN struggles to provide relevant results when applied on its own.

Thus, our method implements an ensemble between the F-CNN and the O-CNN. However, since a comparison among an ensemble method and non-ensemble approaches would not be fair, we included the O-CNN classification to compose an ensemble with the other compared methods. These results are shown in Table 10.

It can be noted that merging the classification results of both CNN not only improves the accuracy of the F-CNN, but also enhances the performance of the O-CNN. When compared to the other techniques, the proposed method provided better accuracies in all datasets. The LG dataset was the only one where the results obtained by our method could be matched by other techniques. In this case, the same accuracy value of 99.62% was obtained by PERC, LAC and the FNN. Besides, a significant difference among the compared techniques was indicated according to the Friedman test ($P_k < 0.0001$ for $\alpha = 0.05$) in all pairwise comparisons (Conover). Our method also provided the highest average accuracy (96.8%) and smallest standard deviation (4.334), as can be seen on the graph presented on Figure 10.

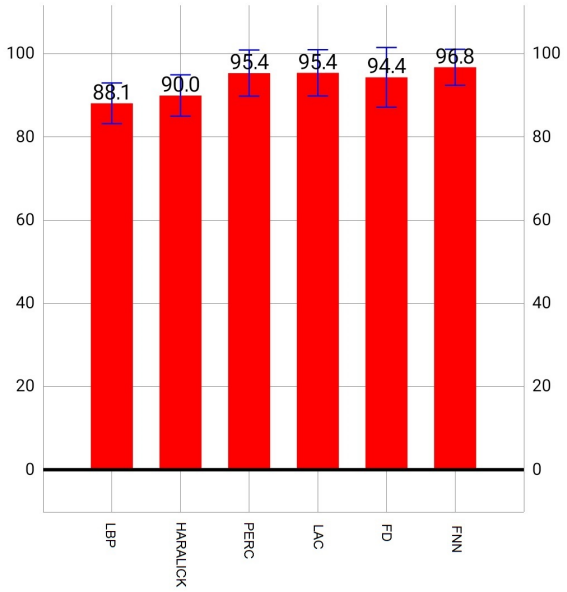

Figure 10: Average accuracy of the evaluated classification ensemble between the O-CNN and other techniques, applied to the five tested datasets.

An overview of the results obtained with the FNN in relation to other approaches in the context of histology image classification is shown in Table 11. It can be noted that the methods that provided the best results on each classification task applied both deep learning (DL) and handcrafted (HC) features. Regarding the FNN, we were able to verify that its performance is compatible with recently published methods. Breast and colorectal cancer

classification remains as a challenging task in computer vision, since few methods were able to obtain accuracies above 95% when classifying these type of images. Nevertheless the FNN was able to achieve a remarkable 99.39% accuracy, ranking first among the compared methods in colorectal cancer classification.

6. Conclusion

In this paper, we proposed an approach (FNN) that consists on the ensemble of two CNN, wherein one of these receives as input images generated from fractal features, to classify different categories of histological images. We showed that our proposal was able to provide relevant results, with accuracies above 89%, for all tested histopathology challenges. Also, accuracies greater than 99% were obtained for three out of the five evaluated datasets (CR, LG and LA). Besides, we achieved these results with a training time shorter than the required for other approaches such as [64, 51, 29] to obtain similar performances. Therefore, we believe our proposal contributes to this research area not only due to its adaptability to different types of histology tissue and relatively low computing cost, but mainly due to the applied feature vectors reshaping concept that allows the combined use of fractal features and CNN. This approach has not yet been deeply explored and could provide new insights on the combined power of handcrafted features and deep learning. Nevertheless, there is still room for improvement, specially in regard to the UCSB dataset classification, wherein hyper-parameter tuning could play a major role to improve the model's accuracy.

For future works, we propose the application of the FNN on other types of histology tissue images, a study for optimizing the F-CNN and the O-CNN parameters, the inclusion of fractal global features in the classification ensemble and a deeper analysis of the fractal features reshaping procedure, *e.g.* experimenting different ways to dispose the features or generating images using a different 3-channel color model.

7. Acknowledgment

This study was financed in part by the Coordenação de Aperfeiçoamento de Pessoal de Nível Superior - Brasil (CAPES) - Finance Code 001 and by the Programa Institucional de Internacionalização (PRINT/CAPES, Brazil), project #88882.461704/2019-01. The authors gratefully acknowledge the

Table 11: Overview of the accuracy values obtained by different approaches in the context of histology image classification.

Images	Method	Approach	Accuracy
NHL	[6]	DL+HC	99,10%
	[24]	DL	97,96%
	[36]	HC	97,00%
	[22]	DL	96,58%
	FNN	DL+HC	**95,55%**
	[47]	HC	86,14%
Breast	[31]	DL+HC	100,00%
	[64]	DL+HC	96,67%
	[13]	DL	94,41%
	[29]	DL	91,00%
	FNN	DL+HC	**89,66%**
	[48]	HC	86,20%
	[44]	DL	84,67%
	[4]	DL	83,30%
	[38]	HC	80,00%
Colorectal	**FNN**	DL+HC	**99,39%**
	[11]	DL	96,97%
	[57]	DL	94,02%
	[51]	DL	93,28%
	[48]	HC	90,90%
	[7]	DL	87,50%
	[5]	DL	85,00%
Liver (gender)	[39]	DL+HC	100,00%
	[12]	HC	100,00%
	FNN	DL+HC	**99,62%**
	[3]	DL	99,10%
Liver (age)	[39]	DL+HC	100,00%
	[12]	HC	100,00%
	FNN	DL+HC	**99,62%**
	[3]	DL	98,20%

financial support of National Council for Scientific and Technological Development CNPq (Grant #427114/2016-0, Grant #304848/2018-2, Grant #430965/2018-4 and Grant #313365/2018-0) and the State of Minas Gerais

Research Foundation - FAPEMIG (Grant #APQ-00578-18).

References

[1] Aličković, E., Subasi, A., 2017. Breast cancer diagnosis using ga feature selection and rotation forest. Neural Computing and Applications 28 (4), 753–763.

[2] Amalina, N. N., Ramadhani, K. N., Sthevanie, F., 2019. Nuclei detection and classification system based on speeded up robust feature (surf). EMITTER International Journal of Engineering Technology 7 (1), 1–13.

[3] Andrearczyk, V., Whelan, P. F., 2017. Deep learning for biomedical texture image analysis. In: Proceedings of the Irish Machine Vision & Image Processing Conference. Irish Pattern Recognition & Classification Society (IPRCS).

[4] Araújo, T., Aresta, G., Castro, E., Rouco, J., Aguiar, P., Eloy, C., Polónia, A., Campilho, A., 2017. Classification of breast cancer histology images using convolutional neural networks. PloS one 12 (6).

[5] Awan, R., Al-Maadeed, S., Al-Saady, R., Bouridane, A., 2019. Glandular structure-guided classification of microscopic colorectal images using deep learning. Computers & Electrical Engineering, 106450.

[6] Bai, J., Jiang, H., Li, S., Ma, X., 2019. Nhl pathological image classification based on hierarchical local information and googlenet-based representations. BioMed research international 2019.

[7] Bentaieb, A., Hamarneh, G., 2018. Adversarial stain transfer for histopathology image analysis. IEEE transactions on medical imaging 37 (3), 792–802.

[8] Bird, N., Perrier, E., 2010. Multiscale percolation properties of a fractal pore network. Geoderma 160 (1), 105–110.

[9] Chollet, F., 2017. Xception: Deep learning with depthwise separable convolutions. In: Proceedings of the IEEE conference on computer vision and pattern recognition. pp. 1251–1258.

[10] Cireşan, D. C., Giusti, A., Gambardella, L. M., Schmidhuber, J., 2013. Mitosis detection in breast cancer histology images with deep neural networks. In: International conference on medical image computing and computer-assisted intervention. Springer, pp. 411–418.

[11] Dabass, M., Vig, R., Vashisth, S., 2019. Five-grade cancer classification of colon histology images via deep learning. In: Communication and Computing Systems: Proceedings of the 2nd International Conference on Communication and Computing Systems (ICCCS 2018), December 1-2, 2018, Gurgaon, India. CRC Press, p. 18.

[12] Di Ruberto, C., Putzu, L., Arabnia, H., Quoc-Nam, T., 2016. A feature learning framework for histology images classification. In: Emerging trends in applications and infrastructures for computational biology, bioinformatics, and systems biology: systems and applications. Elsevier Press, pp. 37–48.

[13] Feng, Y., Zhang, L., Yi, Z., 2018. Breast cancer cell nuclei classification in histopathology images using deep neural networks. International journal of computer assisted radiology and surgery 13 (2), 179–191.

[14] Gelasca, E. D., Byun, J., Obara, B., Manjunath, B., Oct 2008. Evaluation and benchmark for biological image segmentation. In: IEEE International Conference on Image Processing.

[15] Ghanbarian, B., Hunt, A. G., Skinner, T. E., Ewing, R. P., 2015. Saturation dependence of transport in porous media predicted by percolation and effective medium theories. Fractals 23 (01), 1540004.

[16] He, K., Zhang, X., Ren, S., Sun, J., 2016. Deep residual learning for image recognition. In: Proceedings of the IEEE conference on computer vision and pattern recognition. pp. 770–778.

[17] Howlader, N., Noone, A., Krapcho, M., Miller, D., Bishop, K., Kosary, C., Yu, M., Ruhl, J., Tatalovich, Z., Mariotto, A., et al., 2017. Seer cancer statistics review, 1975-2014, national cancer institute. Bethesda, MD, 1–12.

[18] Huang, Q., Zhang, F., Li, X., 2018. Machine learning in ultrasound computer-aided diagnostic systems: a survey. BioMed research international 2018.

[19] Ilse, M., Tomczak, J. M., Welling, M., 2018. Attention-based deep multiple instance learning. In: 35th International Conference on Machine Learning, ICML 2018. International Machine Learning Society (IMLS), pp. 3376–3391.

[20] Ivanovici, M., Richard, N., 2009. The lacunarity of colour fractal images. In: Image Processing (ICIP), 2009 16th IEEE International Conference on. IEEE, pp. 453–456.

[21] Ivanovici, M., Richard, N., 2011. Fractal dimension of color fractal images. IEEE Transactions on Image Processing 20 (1), 227–235.

[22] Janowczyk, A., Madabhushi, A., 2016. Deep learning for digital pathology image analysis: A comprehensive tutorial with selected use cases. Journal of pathology informatics 7.

[23] Japkowicz, N., Shah, M., 2011. Evaluating learning algorithms: a classification perspective. Cambridge University Press.

[24] Jiang, C., Su, J., 2018. Gabor binary layer in convolutional neural networks. In: 2018 25th IEEE International Conference on Image Processing (ICIP). IEEE, pp. 3408–3412.

[25] Jiang, H., Li, Z., Li, S., Zhou, F., 2018. An effective multi-classification method for nhl pathological images. In: 2018 IEEE International Conference on Systems, Man, and Cybernetics (SMC). IEEE, pp. 763–768.

[26] Jiang, Y., Chen, L., Zhang, H., Xiao, X., 2019. Classification of h&e stained breast cancer histopathology images based on convolutional neural network. In: Journal of Physics: Conference Series. Vol. 1302. IOP Publishing, p. 032018.

[27] Jothi, J. A. A., Rajam, V. M. A., 2017. A survey on automated cancer diagnosis from histopathology images. Artificial Intelligence Review 48 (1), 31–81.

[28] Juefei-Xu, F., Naresh Boddeti, V., Savvides, M., 2017. Local binary convolutional neural networks. In: Proceedings of the IEEE conference on computer vision and pattern recognition. pp. 19–28.

[29] Kausar, T., Wang, M., Idrees, M., Lu, Y., 2019. Hwdcnn: Multi-class recognition in breast histopathology with haar wavelet decomposed image based convolution neural network. Biocybernetics and Biomedical Engineering 39 (4), 967–982.

[30] Krizhevsky, A., Sutskever, I., Hinton, G. E., 2012. Imagenet classification with deep convolutional neural networks. In: Advances in neural information processing systems. pp. 1097–1105.

[31] Li, Y., Xie, X., Shen, L., Liu, S., 2019. Reverse active learning based atrous densenet for pathological image classification. BMC bioinformatics 20 (1), 445.

[32] Liu, L., Chen, J., Fieguth, P., Zhao, G., Chellappa, R., Pietikainen, M., 2018. A survey of recent advances in texture representation. arXiv preprint arXiv:1801.10324 3.

[33] Lumini, A., Nanni, L., 2018. Convolutional neural networks for atc classification. Current pharmaceutical design 24 (34), 4007–4012.

[34] Mahbod, A., Ellinger, I., Ecker, R., Smedby, Ö., Wang, C., 2018. Breast cancer histological image classification using fine-tuned deep network fusion. In: International Conference Image Analysis and Recognition. Springer, pp. 754–762.

[35] Mandelbrot, B. B., 1975. Les objets fractals: forme, hasard et dimension.

[36] Martins, A. S., Neves, L. A., Faria, P. R., Tosta, T. A., Bruno, D. O., Longo, L. C., do Nascimento, M. Z., 2019. Colour feature extraction and polynomial algorithm for classification of lymphoma images. In: Iberoamerican Congress on Pattern Recognition. Springer, pp. 262–271.

[37] Mohammed, M. A., Al-Khateeb, B., Rashid, A. N., Ibrahim, D. A., Ghani, M. K. A., Mostafa, S. A., 2018. Neural network and multi-fractal dimension features for breast cancer classification from ultrasound images. Computers & Electrical Engineering 70, 871–882.

[38] Mueller, J. L., Gallagher, J. E., Chitalia, R., Krieger, M., Erkanli, A., Willett, R. M., Geradts, J., Ramanujam, N., 2016. Rapid staining and imaging of subnuclear features to differentiate between malignant and

benign breast tissues at a point-of-care setting. Journal of cancer research and clinical oncology 142 (7), 1475–1486.

[39] Nanni, L., Brahnam, S., Ghidoni, S., Maguolo, G., 2019. General purpose (genp) bioimage ensemble of handcrafted and learned features with data augmentation. arXiv preprint arXiv:1904.08084.

[40] Nanni, L., Ghidoni, S., Brahnam, S., 2017. Handcrafted vs. non-handcrafted features for computer vision classification. Pattern Recognition 71, 158–172.

[41] Nikolaidis, N., Nikolaidis, I., Tsouros, C., 2011. A variation of the box-counting algorithm applied to colour images. arXiv preprint arXiv:1107.2336.

[42] on Aging, N. I., Accessed: 2020-05-04. The atlas of gene expression in mouse aging project (agemap). `https://ome.grc.nia.nih.gov/iicbu2008/agemap/index.html`.

[43] Orlov, N. V., Chen, W. W., Eckley, D. M., Macura, T. J., Shamir, L., Jaffe, E. S., Goldberg, I. G., 2010. Automatic classification of lymphoma images with transform-based global features. IEEE Transactions on Information Technology in Biomedicine 14 (4), 1003–1013.

[44] Papastergiou, T., Zacharaki, E. I., Megalooikonomou, V., 2018. Tensor decomposition for multiple-instance classification of high-order medical data. Complexity 2018.

[45] Rakhlin, A., Shvets, A., Iglovikov, V., Kalinin, A. A., 2018. Deep convolutional neural networks for breast cancer histology image analysis. In: International Conference Image Analysis and Recognition. Springer, pp. 737–744.

[46] Ribeiro, M. G., Neves, L. A., do Nascimento, M. Z., Roberto, G. F., Martins, A. S., Tosta, T. A. A., 2019. Classification of colorectal cancer based on the association of multidimensional and multiresolution features. Expert Systems with Applications 120, 262–278.

[47] Ribeiro, M. G., Neves, L. A., Roberto, G. F., Tosta, T. A., Martins, A. S., do Nascimento, M. Z., 2018. Analysis of the influence of color normalization in the classification of non-hodgkin lymphoma images.

In: 2018 31st SIBGRAPI Conference on Graphics, Patterns and Images (SIBGRAPI). IEEE, pp. 369–376.

[48] Roberto, G. F., Nascimento, M. Z., Martins, A. S., Tosta, T. A., Faria, P. R., Neves, L. A., 2019. Classification of breast and colorectal tumors based on percolation of color normalized images. Computers & Graphics 84, 134–143.

[49] Roberto, G. F., Neves, L. A., Nascimento, M. Z., Tosta, T. A., Longo, L. C., Martins, A. S., Faria, P. R., 2017. Features based on the percolation theory for quantification of non-hodgkin lymphomas. Computers in biology and medicine 91, 135–147.

[50] Russakovsky, O., Deng, J., Su, H., Krause, J., Satheesh, S., Ma, S., Huang, Z., Karpathy, A., Khosla, A., Bernstein, M., et al., 2015. Imagenet large scale visual recognition challenge. International journal of computer vision 115 (3), 211–252.

[51] Sena, P., Fioresi, R., Faglioni, F., Losi, L., Faglioni, G., Roncucci, L., 2019. Deep learning techniques for detecting preneoplastic and neoplastic lesions in human colorectal histological images. Oncology Letters 18 (6), 6101–6107.

[52] Shamir, L., Orlov, N., Eckley, D. M., Macura, T. J., Goldberg, I. G., 2008. Iicbu 2008: a proposed benchmark suite for biological image analysis. Medical & biological engineering & computing 46 (9), 943–947.

[53] Simon, O., Yacoub, R., Jain, S., Tomaszewski, J. E., Sarder, P., 2018. Multi-radial lbp features as a tool for rapid glomerular detection and assessment in whole slide histopathology images. Scientific reports 8 (1), 2032.

[54] Sirinukunwattana, K., Pluim, J. P., Chen, H., Qi, X., Heng, P.-A., Guo, Y. B., Wang, L. Y., Matuszewski, B. J., Bruni, E., Sanchez, U., et al., 2017. Gland segmentation in colon histology images: The glas challenge contest. Medical image analysis 35, 489–502.

[55] Szegedy, C., Vanhoucke, V., Ioffe, S., Shlens, J., Wojna, Z., 2016. Rethinking the inception architecture for computer vision. In: Proceedings of the IEEE conference on computer vision and pattern recognition. pp. 2818–2826.

[56] Tan, C., Sun, F., Kong, T., Zhang, W., Yang, C., Liu, C., 2018. A survey on deep transfer learning. In: International conference on artificial neural networks. Springer, pp. 270–279.

[57] Tavolara, T. E., Niazi, M. K. K., Arole, V., Chen, W., Frankel, W., Gurcan, M. N., 2019. A modular cgan classification framework: Application to colorectal tumor detection. Scientific Reports 9 (1), 1–8.

[58] Tosta, T. A. A., Faria, P. R., Neves, L. A., do Nascimento, M. Z., 2017. Computational method for unsupervised segmentation of lymphoma histological images based on fuzzy 3-partition entropy and genetic algorithm. Expert Systems with Applications 81, 223–243.

[59] Wang, H., Roa, A. C., Basavanhally, A. N., Gilmore, H. L., Shih, N., Feldman, M., Tomaszewski, J., Gonzalez, F., Madabhushi, A., 2014. Mitosis detection in breast cancer pathology images by combining handcrafted and convolutional neural network features. Journal of Medical Imaging 1 (3), 034003.

[60] Wang, Y., Huang, F., Zhang, Y., Zhang, R., Lei, B., Wang, T., 2019. Breast cancer image classification via multi-level dual-network features and sparse multi-relation regularized learning. In: 2019 41st Annual International Conference of the IEEE Engineering in Medicine and Biology Society (EMBC). IEEE, pp. 7023–7026.

[61] Wang, Y., Lei, B., Elazab, A., Tan, E.-L., Wang, W., Huang, F., Gong, X., Wang, T., 2020. Breast cancer image classification via multi-network features and dual-network orthogonal low-rank learning. IEEE Access 8, 27779–27792.

[62] Xu, H., Yan, J., Persson, N., Lin, W., Zha, H., 2017. Fractal dimension invariant filtering and its cnn-based implementation. In: Proceedings of the IEEE Conference on Computer Vision and Pattern Recognition. pp. 3491–3499.

[63] Yamashita, R., Nishio, M., Do, R. K. G., Togashi, K., 2018. Convolutional neural networks: an overview and application in radiology. Insights into Imaging, 1–19.

[64] Yu, C., Chen, H., Li, Y., Peng, Y., Li, J., Yang, F., 2019. Breast cancer classification in pathological images based on hybrid features. Multimedia Tools and Applications, 1–21.